https://doi.org/10.48048/tis.2022.4430

Detailed Analysis of Crystal Structure and Optical Properties of Green Synthesized Nanoparticles: Application for Photocatalyst Degradation of Methylene Blue

Arul Vathana Selestin[1,2,*], Amudhavalli Karuppiah[2], Vinoline Golda Thanapalan[1,2] and Infant Francita Fonseka Christopher[1,2]

[1]Department of Physics, V.O. Chidambaram College, Thoothukudi 628 008, Tamilnadu, India
[2]Manonmaniam Sundaranar University, Abishekapatti, Tirunelveli 627012, Tamilnadu, India

([*]Corresponding author's e-mail: arulvathana04@gmail.com)

Received: 29 May 2022, Revised: 27 July 2022, Accepted: 25 August 2022, Published: 11 November 2022

Abstract

We report the green chemistry reduction approach method for the synthesis of Manganese Oxide nanoparticles (MnO NPs), Copper Oxide nanoparticles (CuO NPs) and Manganese-doped Copper Oxide nanoparticles (Mn-doped CuO Nps). Aqueous extract from the seeds was used as reducing and capping agents. The detailed crystal structure analysis was investigated; crystallite size, crystallinity, morphological index, x-ray density, bulk density, specific surface area, porosity, Lorentz factor, Lorentz polarization factor and other parameters were calculated. Simple EDX mapping reveals the presence of Mn, Cu, O and C. FTIR analysis was used to determine the bond length of a nanocomposite. In the visible area, nanoparticles have higher optical absorption, with bandgaps varying from 1.79 (MnO), 2.18 eV (CuO) and 1.72 eV (Mn-doped CuO). After 90 min, the photodegradation rate of Mn-doped CuO nanocatalysts was 93.73 % while using a smaller amount of catalyst (0.1 g) at pH 7. The pseudo-first-order MB photocatalytic decomposition kinetic model has a high correlation coefficient value ($R^2 > 0.95$). It was found that Mn-doped CuO NPs have higher photocatalytic efficiency and can be used as potential photocatalysts for industrial dye degradation.

Keywords: Green synthesis, Metallic oxide nanoparticles, Crystal structure analysis, Bond length, Photodegradation

Introduction

The primary global problem for the 21st century is to provide and ensure safe water for the entire ecosystem. Water contamination is the main factor in rapid industrialization rise. Dyes are an organic chemistry class widely utilized in textiles, the food sector and printing. Dye effluent has a significant detrimental impact on the environment, with the majority of them being highly toxic and non-biodegradable [1,2]. A range of materials and technologies have been established to successfully separate and degrade this waste from the environment. At present, photocatalysis provides for the efficient degradation of a wide range of organic contaminants in aqueous wastes. This method depends on the employment of semiconductor materials, which, when activated with suitable light sources, create numerous reactive species [3]. During the photocatalytic oxidation process, the organic pollutants are eliminated in the presence of semiconductor photocatalysts (such as TiO_2, ZnO, CdS, MnO, CuO, Co_3O_4 and WO_3), an energetic light source and an oxidizing agent like oxygen or air. To the best of our knowledge, only photons with energies greater than the bandgap energy (ΔE) can excite valence band (VB) electrons, potentially stimulating interactions with organic contaminants. When photons with energies less than ΔE or with longer wavelengths are absorbed, the energy usually dissipates as heat. A positive hole (h^+) in the valence band and an electron (e^-) in the conduction band (CB) form on the photocatalytic surface when it is adequately illuminated. The electron in the conduction band reduces the oxygen adsorbed on the photocatalyst, while the positive hole immediately oxidizes the pollutant or water to generate the hydroxyl radical, $OH^{\bullet}$. In the photocatalytic destruction of pollutants, the e^- and h^+ recombination rate increases when oxygen reduction and pollutant oxidation do not take place simultaneously. This is because there is an electron accumulation in the conduction band [4]. The cation doping can further activate a surface for usage in catalytic reactions [5]. Surface area and surface defects are essential in enhancing metal oxide photocatalytic activity. This is

because doping metal oxides with metals and/or transition metals in surface flaws changes optical and electrical properties and moves optical absorption towards the visible range [6].

This study shows how to use a green precipitation approach to create Mn, Cu and Mn-doped Cu oxide nanoparticles. The structural, optical and morphological analyses of synthesized products were carried out. The synthesis of Mn-doped CuO NPs was also analyzed for methylene blue photodegradation.

Materials and methods

Chemicals and reagents

All of the reagents used in the study were of analytical grade. Manganese nitrate [$Mn(No_3)_2 \cdot 4H_2O$], Copper nitrate [$Cu(No_3)_2 \cdot 3H_2O$], and Methylene blue dye were purchased from Sigma Aldrich, a chemical supplier. Throughout the research, deionized water was used to prepare the solution.

Preparation of green reducing and stabilizing agent

Bambusa seeds were brought from a nearby store. To eliminate contaminants, the seeds were rinsed in distilled water. Twenty g of seeds were suspended in 100 mL of distilled water to prepare the aqueous extract. The suspension was heated for 20 min at 60 ℃, and then cooled before being filtered (Whatman's No. 1 filter paper). The filtrate (brown color) residue was used for further purposes.

Synthesis of manganese oxide nanoparticles

In 100 mL of deionized water, a 0.01 M manganese nitrate [$Mn(No_3)_2 \cdot 4H_2O$] was dissolved and vigorously stirred. Twenty mL of green extract was added to the prepared solution drop by drop. The entire solution was whirled at 700 rpm for 2 h until it formed a clear solution that could be stored at room temperature for 12 h. The precipitate was rinsed 5 times with water and ethanol to eliminate by-products and unreacted chemicals and then it was dried in a hot air oven for 2 h at 100 ℃ before being annealed in a muffle furnace for 5 h at 500 ℃. The material was ground after calcination and used for analysis and application. A similar approach to that described above was used to synthesize copper oxide nanoparticles.

Synthesis of manganese-doped copper oxide nanoparticles

In 100 mL of deionized water, 0.01 M manganese nitrate [$Mn(No_3)_2 \cdot 4H_2O$] was dissolved and vigorously stirred, and 100 mL of 0.01 M copper nitrate [$Cu(NO_3)_2 \cdot 3H_2O$] in deionized water were synthesized separately to make Mn-doped Cu oxide nanoparticles. After that, dropwise additions of manganese nitrate solution to copper nitrate solution were made for 20 min at room temperature with vigorous stirring. The green extract was then added drop by drop to the solution while it was agitated at 700 rpm. Finally, a dark brown-colored mixture was formed, which was stirred for 3 - 4 h at room temperature before settling for another 12 h. The resultant precipitate was rinsed several times with ethanol and deionized water to eliminate any remaining impurities. It was then dried for 2 h at 100 ℃ before being crushed into powder. This powder was then calcined at 500 ℃ for 5 h to produce finely divided $Cu_2Mn_3O_8$ nanoparticles. The dry powder is crushed with an agate mortar after calcination and is utilized for analysis and application.

Photocatalytic activity procedure

The photocatalytic activity of Mn-doped Cu oxide nanoparticles was investigated by studying the photodegradation of MB dye solution in the presence of sunlight. To make the reaction suspension, 0.1 g of catalyst was added to 25 mL of each MB dye solution under natural conditions (pH 7) at an initial concentration of 9 ppm and placed in 250 mL of open borosil glasses. The degraded dye solutions were centrifuged at 1,000 rpm for 10 min to measure UV-visible absorbance. As the irradiation period rises, the absorption peaks of the MB dye gradually decrease. The destruction of the dye molecules' homo and heteropolar aromatic rings reduced the absorption of the combined solution [7]. The rate of photodegradation of methylene blue (MB) was calculated using Eq. (1) [8].

$$Degradation\ (\%) = \frac{A_0 - A_t}{A_0} * 100 \quad (1)$$

A_0 denotes the absorbance of illumination; A_t denotes the absorbance of the solution reaction illuminate t. The pseudo-first-order kinetics can be represented by the following Eq. (2):

$$In\left(\frac{C_t}{C_0}\right) = -kt \quad (2)$$

where C_t is the concentration at time t and C_0 is the initial concentration of the dye, K is the rate constant of a pseudo- first-order reaction.

Results and discussion

Structural characteristics

XRD is a widely utilized technique for studying structural features of powder crystalline solid materials, as well as the lattice parameters of manufactured pure and metal-doped CuO. Cu-K radiation with a wavelength of 1.54060 Å was used to collect XRD data. **Figure 1** depicts the XRD graph of all as-synthesized nanomaterials. The diffraction peaks of pure Mn_2O_3 nanoparticle synthesis at 2θ = 32.96 and 55.18 ° correspond to (2 2 2) (4 4 0) and match the cubic structure of JCPDS Card No. 89-4836 (**Figure 1a**). The diffraction pattern has a few weak peaks, indicating that the produced nanoparticles are not entirely crystalline.

CuO NPs Confirmation was indexed at 2θ = 35.49, 38.73, 48.73, 53.45, 58.33, 61.52, 66.25 and 68.09 ° which correspond to monoclinic structured CuO (h k l) planes (0 0 2) (1 1 1) ($\bar{2}$ 0 2) (0 2 0) (2 0 2) ($\bar{1}$ 1 3) ($\bar{3}$ 1 1) and ($\bar{2}$ 2 0) JCPDS Card No. 45-0937. The high peaks show that the nanoparticles are entirely crystalline (**Figure 1b**). The strong peaks imply that the nanoparticles were synthesized in a crystalline form.

The most prominent diffraction peak in Mn-doped CuO nanocrystallites appears at around 34.19 ° and corresponds to the ($\bar{3}$ 1 1) crystal plane, while lower intensities appear at around 2θ = 24.57, 37.11, 39.69, 46.30, 51.01, 58.13 and 65.26 ° corresponds to ($\bar{1}$ 1 1), (2 2 0), ($\bar{2}$ 2 1), (2 0 2), (5 1 0), ($\bar{3}$ 3 1) and (1 3 2), respectively, planes of $Cu_2Mn_3O_8$ matched with the monoclinic structure of JCPDS Card No. 70-0395 (**Figure 1c**). As seen in the **Figure 1c**, the XRD patterns of undoped and Mn-doped CuO differ [10]. In the transition, metal-doped CuO nanocrystals had a minor shift in broad peaks when compared to undoped Mn and CuO nanocrystals, and this slight shift in intensity might be attributed to the presence of dopant metal. The peak location differs slightly from that of pure in the case of doping. Mn_2O_3 and CuO have crystallite sizes of 8 and 49.83 nm, respectively, while metal doping into CuO reduces the average crystalline size of doped materials $Cu_2Mn_3O_8$ = 24.84 nm. Debye Scherrer's relation at full width half maximum (FWHM) has been used to estimate the average size of crystallites (D).

$$D = \frac{k\lambda}{\beta cos\theta} \tag{3}$$

where D is the average crystallite size and k is Scherrer's constant, a proportionality constant that depends on the crystalline structure's form and size distribution. It is generally assumed that k = 0.9, λ = 1.54056, β is FWHM, and is the angle of diffraction or Bragg's angle measured from the 2θ scale.

The lattice parameters were derived using the following relationship (4,5,6) [11].

$$\frac{1}{d^2} = \frac{h^2+k^2+l^2}{a^2} \tag{4}$$

$$\frac{1}{d^2} = \frac{h^2+k^2}{a^2} + \frac{l^2}{c^2} \tag{5}$$

$$\frac{1}{d^2} = \frac{h^2}{a^2} + \frac{k^2}{b^2} + \frac{l^2}{c^2} \tag{6}$$

where *h*, *k* and *l* are miller indices, *a*, *b* and *c* are lattice parameters and d is interplanar spacing, Bragg's law is used to evaluate d-spacing(interplanar spacing) [12] which is given as.

$$2dsin\theta = n\lambda \tag{7}$$

where d stands for d-spacing, λ is the wavelength of the X-ray beam (1.54056 Å), θ is the diffraction angle acquired from XRD data, and n is an integer indicating the order of diffraction (n = 1 for first-order diffraction). Eq. (7) is used to calculate d-spacing, it may be used in Eqs. (4) - (6) to get the lattice parameters a, b and c.

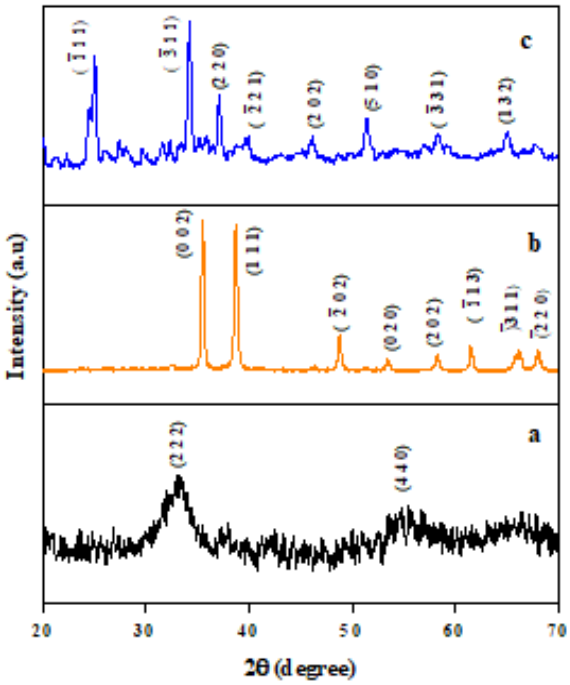

Figure 1 The magnified characteristic peaks of a) Mn_2O_3, b) CuO, c) Mn-doped CuO

Table 1 Crystalline parameters from XRD analysis

Samples	2θ (degree)	d-spacing (Å)	Crystallite size (nm)	Lattice Parameters			
	For most intense peak			a (Å)	b (Å)	c (Å)	V (Å)
Mn_2O_3	32.96	2.71	10.31	9.406	9.406	9.406	832.18
CuO	35.49	2.52	31.17	4.685	3.425	5.13	81.2
$Cu_2Mn_3O_8$	34.19	2.61	24.84	9.695	5.635	4.912	216.10

Crystallinity of sample

XRD data straightforwardly calculated the percentage of crystallinity size. Without any further procedures, XRD includes the scattering of both amorphous and crystalline phases. The XRD method uses the area of both amorphous and crystalline peaks to get an extremely precise and accurate percentage of crystallinity [13]. The following formula (8) was used to calculate the crystallinity.

$$Percentage\ crystallinity = \frac{Total\ area\ of\ crystalline\ peaks}{Total\ area\ of\ all\ the\ peaks(amorphous + crystalline)} \quad (8)$$

Table 2 depicts the crystallinity of MnO, CuO and Mn-doped CuO NPs. The nanopowders had higher crystallinity, indicating that they were crystalline.

Morphological index (M.I)

The high nanocrystalline structure of peaks causes sharper crystalline peaks in the XRD spectrum. The FWHM of the XRD data is used to calculate the Morphology Index (M.I). M.I. is directly correlated with the average crystallite size of nanopowder and is inversely correlated with specific surface area (SSA) [14]. The morphological index of nanomaterials was computed using the following formula (9);

$$M.I = \frac{FWHM_h}{FWHM_h + FWHM_P} \quad (9)$$

where $FWHM_h$ is the full-width half maxima of the highest and $FWHM_p$ is the particular crystalline peaks, respectively. The morphological index for undoped and doped metal oxide nanoparticles is displayed in **Table 2**.

Number of unit cells

The number of unit cells was calculated using the following relationship (10);

$$n = \pi \times (\frac{4}{3}) \times (\frac{D}{2})^3 \times \frac{1}{V} \quad (10)$$

where n is the number of unit cells, D is the crystallite size (as calculated by Debye Scherer's formula), and V is the unit cell volume. The number of unit cells (n)×10^4 is shown in **Table 2** [15].

X-ray density

The following relationship was used to calculate the X-ray density *(ρ_{XRD})* of nanopowders.

$$\rho_{XRD} = \frac{NM_W}{N_A V} \quad (11)$$

where N denotes for the number of atoms in the cell lattice, Mw for the molecular weight of undoped and doped metal oxide nanoparticles (which varies depending on the sample), NA for Avogadro's number ($6.022 \times 10^{23}\ mol^{-1}$),, and V for the volume of the unit cell. **Table 2** shows the X-ray density of undoped and doped metal oxide nanoparticles in g/cm^3.

Bulk density

The bulk density of nanopowder (ρ_{bulk}) is used to define the mass per unit volume of the pellet. It can be calculated as follows (12):

$$\rho_{bulk} = \frac{m}{V} = \frac{m}{\frac{4}{3}\pi r^3} \quad (12)$$

where m is mass, V is volume, and r is the radius of the pellet [16]. **Table 2** shows the bulk densities of the samples Mn_2O_3, CuO and $Cu_2Mn_3O_8$ in g/m^3.

Specific surface area (SSA)

SSA is a material property that has a significant role in adsorption, surface reactions and heterogeneous catalysis. The Brunauer-Emmett-Teller formula was used to determine the specific surface.

$$SSA = \frac{6}{\rho_{XRD} \times D} \quad (13)$$

where ρ_{XRD} is material in g/cm^3 and *D* (m) is the average crystallite size of nanopowder [17]. **Table 2** shows the estimated SSA in m^2/g.

Table 2 Morphological Index, X-ray density, Bulk density and Specific surface area

Samples	Percentage Crystallinity	Morphological Index (M.I)	Number of unit cells (n)10^4	X-ray density ρ_{XRD} (g/cm^3)	Bulk density ρ_{bulk} (g/cm^3)	Specific Surface Area SSA (m^2/g)
Mn_2O_3	38.91	0.75	0.0321	2.52	0.1468	297.61
CuO	73.64	0.59	7.9743	1.62	0.1192	74.326
$Cu_2Mn_3O_8$	62.4	0.55	6.5067	1.82	0.1404	110.07

Dislocation density

The density of dislocations (δ) implies that defect levels are forming in the lattice structure. The number of dislocation lines per unit volume is used to define defects in nanomaterials; Eq. (14) shows that dislocation density is a sort of topological deformity, and the broadening of the peak is referred to as

crystallite size (D) [18]. The dislocation density (δ) of the sample was estimated using the provided formula (14).

$$\delta = \frac{1}{D^2} \tag{14}$$

The dislocation density of nanoparticles with varying Mn, Cu and Mn-doped Cu metal oxide NPs is represented in **Table 3**.

Porosity

Porosity is a measure of how many pore spaces there are in the lattice structure of a nanopowder. Although porosity cannot be measured directly, it can be estimated using X-rays and bulk densities. It is also a dimensionally ambiguous quantity [19]. It can also be determined using a relationship (15).

$$Porosity\ (P.S) = \left(1 - \frac{\rho_{bulk}}{\rho_{XRD}}\right) \times 100 \tag{15}$$

The percentage of pore space in nanopowders is shown in **Table 3**.

Lorentz factor (LF) and Lorentz polarization factor (LPF)

The peak intensity of diffracted X-rays is equal to the square of the structure factor and the Polarization Lorentz factor. When compared to reflections in the forward or reverse directions, the Lorentz factor reduces the strength of reflections at moderate angles. The Lorentz factor (LF) and Lorentz polarization factor (LFPF) are calculated using Eqs. (16) - (17). The LPF is a trigonometric factor (P_θ) that affects the intensity of X-rays around the diffraction angle. It was calculated by taking the form (geometry) and diffraction for the most extreme peak intensity, Imax, and peak broadness, and it was produced by rephrasing the Thomson Eq. (18) [20].

$$L.F = \frac{1}{4siin^2\theta cos\theta} \tag{16}$$

$$LPF = \frac{(1+cos^2 2\theta)}{sin^2\theta cos\theta} \tag{17}$$

$$P_\theta = \frac{(1+cos^2 2\theta)}{2} \tag{18}$$

The L.F, LPF and P_θ values, calculated, are mentioned in the table (**Table 3**).

Microstrain

Microstrain, or non-uniform strain, causes atoms or unit cells to shift from their typical locations, causing the peak in the XRD spectrum to broaden and it can be caused by dislocation of densities, domain boundaries and surfaces [21]. Nanomaterials frequently experience microstrain, which can be measured as (19).

$$\epsilon = \frac{\beta}{4tan\theta} \tag{19}$$

Table 3 shows the microstrain or non-uniform strain.

Table 3 Dislocation density, Percentage of pore space, Lorentz factor, Micro strain

Samples	**Dislocation Density (lines/nm^2)**	**% Pore space (porosity) P.S**	**Lorentz factor LF**	**Trigonometric (Thomson) Factor P_θ**	**Lorentz polarization factor LPF**	**Micro strain**
Mn_2O_3	0.009392	94.17	3.2396	0.8520	22.081	0.0118
CuO	0.001029	92.66	2.8272	0.8314	18.806	0.0036
$Cu_2Mn_3O_8$	0.001620	92.28	3.0285	0.8421	20.402	0.0041

UV-vis diffuse reflectance spectra (UV-DRS)

Diffused reflectance spectroscopy (DRS) measurements were utilized to investigate the optical characteristics of Mn, Cu and Mn-doped Cu metal oxide nanoparticles. UV-visible analyses of seed extracts of undoped and doped metal oxide nanoparticles were then performed to detect the absorption maxima of biological components involved in reduction and capping. Mn_2O_3 nanoparticles had a broad absorption band with 2 distinct absorption peaks at 277 and 350 nm (**Figure 2(a)**). A distinctive signal at 270 nm validated the production of CuNPs [22]. **Figure 2(b)** shows the distinctive absorption maximum of photosynthesised CuNPs, which has a peak at 326 nm. Cu NPs surface plasmon resonance (SPR) is the main cause of this absorption band. The SPR for CuO NPs can be seen as a strong absorption peak at 250 nm. This is brought on by incident electromagnetic radiation excitation of surface conduction electron oscillation. The SPR band of various Cu colloid forms of nonoxidized Cu NPs was identified as the source of a further weak and broad spectrum in the 320 - 600 nm range [23]. The absorption edge of CuO nanoparticles is observed at 480 nm, whereas the absorption edge of Mn-doped CuO nanoparticles is increased towards higher wavelengths [24]. The bandgap therapy demonstrates that the nanoparticles exhibit semiconductor characteristics and function as active photocatalysts for MB degradation. The bandgap for Mn-doped CuO drops by 1.72 eV when compared to Mn, Cu metal oxide NPs as shown in **Table 4**.

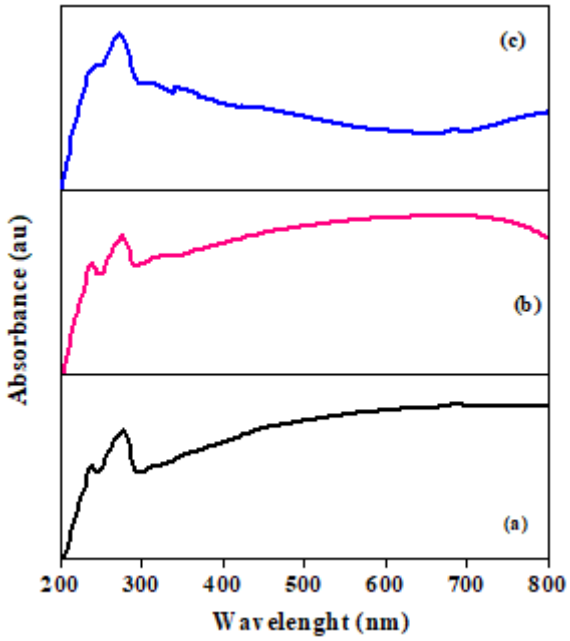

Figure 2 UV-vis-DRS spectra of (a) Mn_2O_3, (b) CuO, (c) Mn-doped CuO.

Table 4 Bandgap Values of undoped and doped NPs.

S. no	Sample	Bandgap (eV)
1	Mn_2O_3	1.79
2	CuO	2.18
3	$Cu_2Mn_3O_8$	1.72

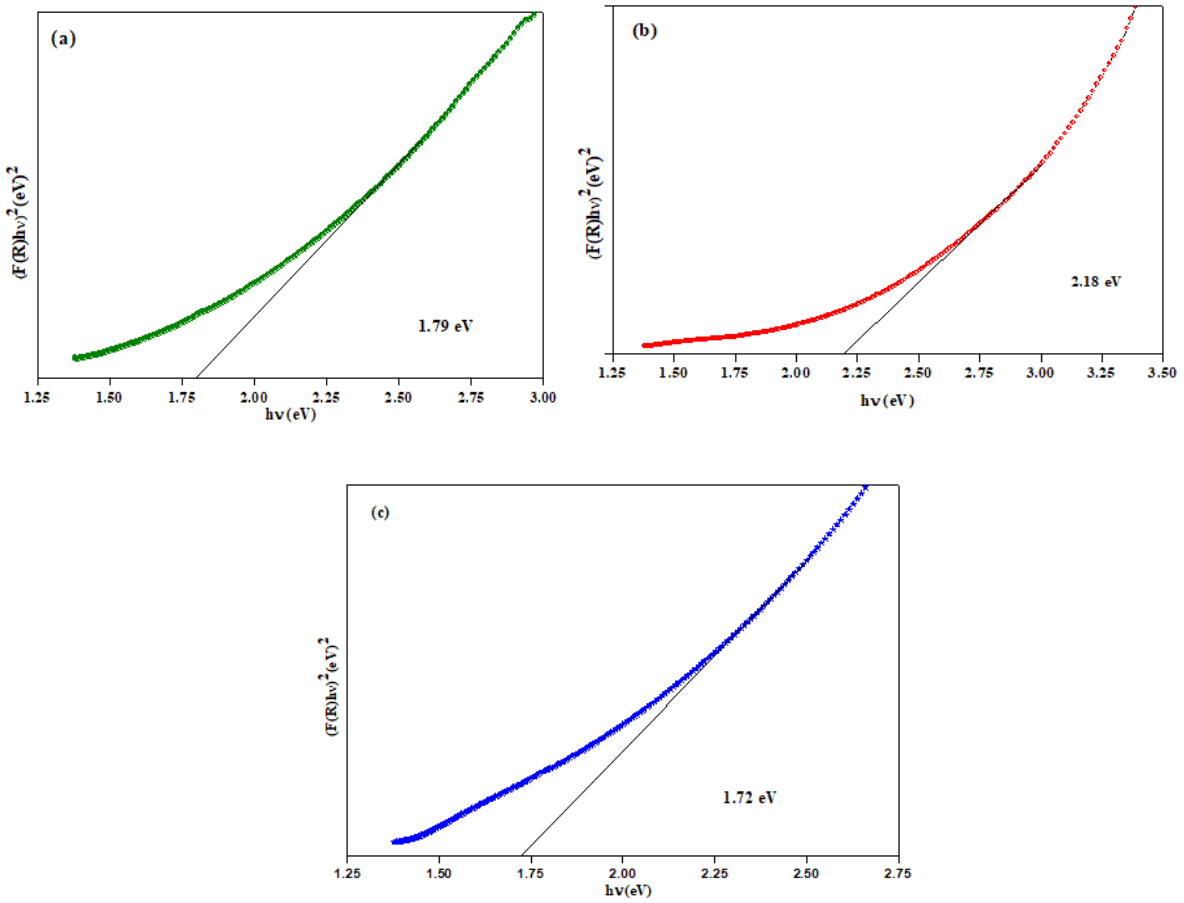

Figure 3 Bandgap (a) Mn_2O_3, (b) CuO, (c) Mn-doped CuO.

Functional group analysis

Fourier transformation infrared spectroscopy (FTIR)

The FT-IR spectrum is used to identify potential biomolecules involved in the capping and effective stability of metal nanoparticles produced from seed extract (**Figure 5**). The peaks at 650 and 520 cm^{-1} are related to O-Mn-O stretching and bending and confirm the creation of MnO_2 nanoparticles [25]. Mn-O FTIR signal at 460 and 580 cm^{-1} [26]. The formation of pure CuO nanoparticles is confirmed by the narrow bands at 457 and 600 cm^{-1} [23]. This suggests that the biological component in the seed extract performs both the role of stabilization and the synthesis of CuO NPSs. 1,010.39 cm^{-1} shows O-C stretching [27] and 1,043 cm^{-1} denotes the C-O group [28]. The peak in the Mn-O wagging mode of vibrations at 426 cm^{-1} [29]. The peaks at 504 cm^{-1} are allied with CuO vibrations of the monoclinic structure. CuO stretching is responsible for the band at 504 cm^{-1} [30]. The dopant Mn-O trembling can be seen at the peak at 608 cm^{-1} [31], while the C-O band peaks at 1,050 cm^{-1} [32]. The peak at 2,977 cm^{-1}, which is related to O-H stretching, may be due to -C-H stretching vibrations at 1,382.96 cm^{-1} [33]. As a result, these findings indicate that green-synthesized NPs are completely capped with biologically active phytomolecules of seed extract with such functional groups.

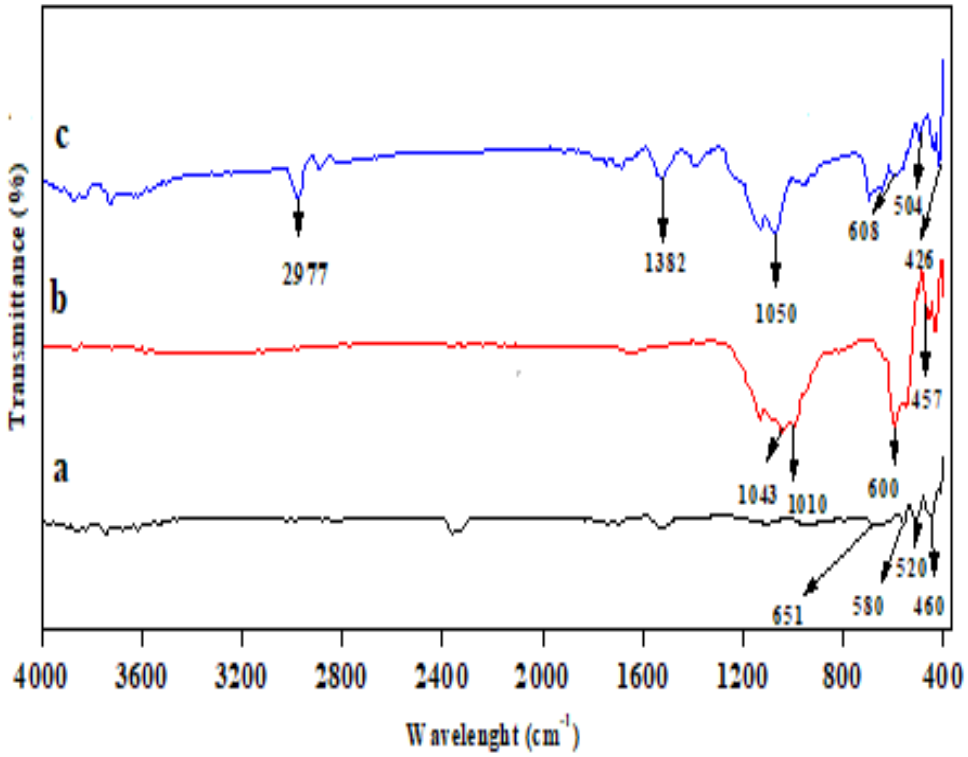

Figure 5 FTIR spectra of (a) Mn_2O_3, (b) CuO, (c) Mn-doped CuO.

Determination of bond length using Badger's rule

The following is Richard M. Badger's formula is used for determining bond length (R) using the force constant (k) (dynes.cm^{-1}): [34]

$$R = \sqrt[3]{\frac{C_{ij}}{k}} + d_{ij} \quad (20)$$

The force constant k is expressed as mega-dynes per centimetre. (1 Nm^{-1} = 0.001 Md.cm^{-1}).

C_{ij} and d_{ij} are the fitting constants that depend on the number of bonded atoms in each period of the periodic table. Mn_2O_3 and CuO have C_{ij} values of 0.50 and 0.50 Å, respectively, and d_{ij} values of 1.06 and 1.06 Å, respectively [35].

Hook's approach was used to calculate the bond's force constant (k), which is a measure of bond stiffness, using the basic harmonic Eq. (21). Shorter bonds have a greater force constant (k) and are therefore more powerful.

$$\nu = \frac{1}{2\pi}\sqrt{\frac{k}{\mu}} \quad (21)$$

where the relation in Eq. (22) is used to calculate the reduced mass (μ) in kg of bound atoms [36].

$$\mu = \frac{m_1 \times m_2}{m_1 + m_2} \quad (22)$$

m_1 and m_2 are the atomic masses of bonded atoms. Eq. (21) is manipulated in the following method Eq. (23) to get the force constant (k, Nm^{-1}) from wavenumbers.

$$k = \nu^2 4\pi^2 c^2 \mu \quad (23)$$

The bond length for Mn-O calculated using Badger's formula was in the range of 2.23 - 2.53 Å (average 2.36 Å). Similarly, the bond length of the Cu-O bond was calculated and found to be between 2.38 and 2.47 Å (average 2.42 Å).

Field emission scanning electron microscopy (FE-SEM) and energy dispersive spectrum (EDS)

FE-SEM images were used to depict the surface morphology of pure and doped transition metal oxide nanoparticles. The morphology of nanoparticles was determined using FE-SEM. The SEM picture of the green-synthesized Mn, Cu and Mn-doped Cu oxide NPs is shown in **Figure 6**. In the SEM the green-synthesized Mn_2O_3 has a cauliflower-like morphology. The SEM scan also indicated that the Mn_2O_3 nanoparticles were uniformly dispersed as shown in **Figure 6a**. According to **Figure 6b**, CuO nanoparticles are greatly distributed with a rod and irregular forms. **Figure 6c** depicts the shift in morphologies observed for Mn-doped CuO nanoparticles. The addition of Mn-doped CuO nanoparticles causes a significant change in the nanostructure of the sample. All of these nanoparticle samples are agglomerated with some crystalline structure. The elemental composition of the produced nanoparticles reveals higher peaks for Mn and Cu indicating that the product is pure and free of contaminants. The peaks corresponding to carbon (C) and oxygen (O) were also clearly visible in the EDS spectrum, confirming the adsorption of biological molecules on the surface of nanoparticles from the seed extract.

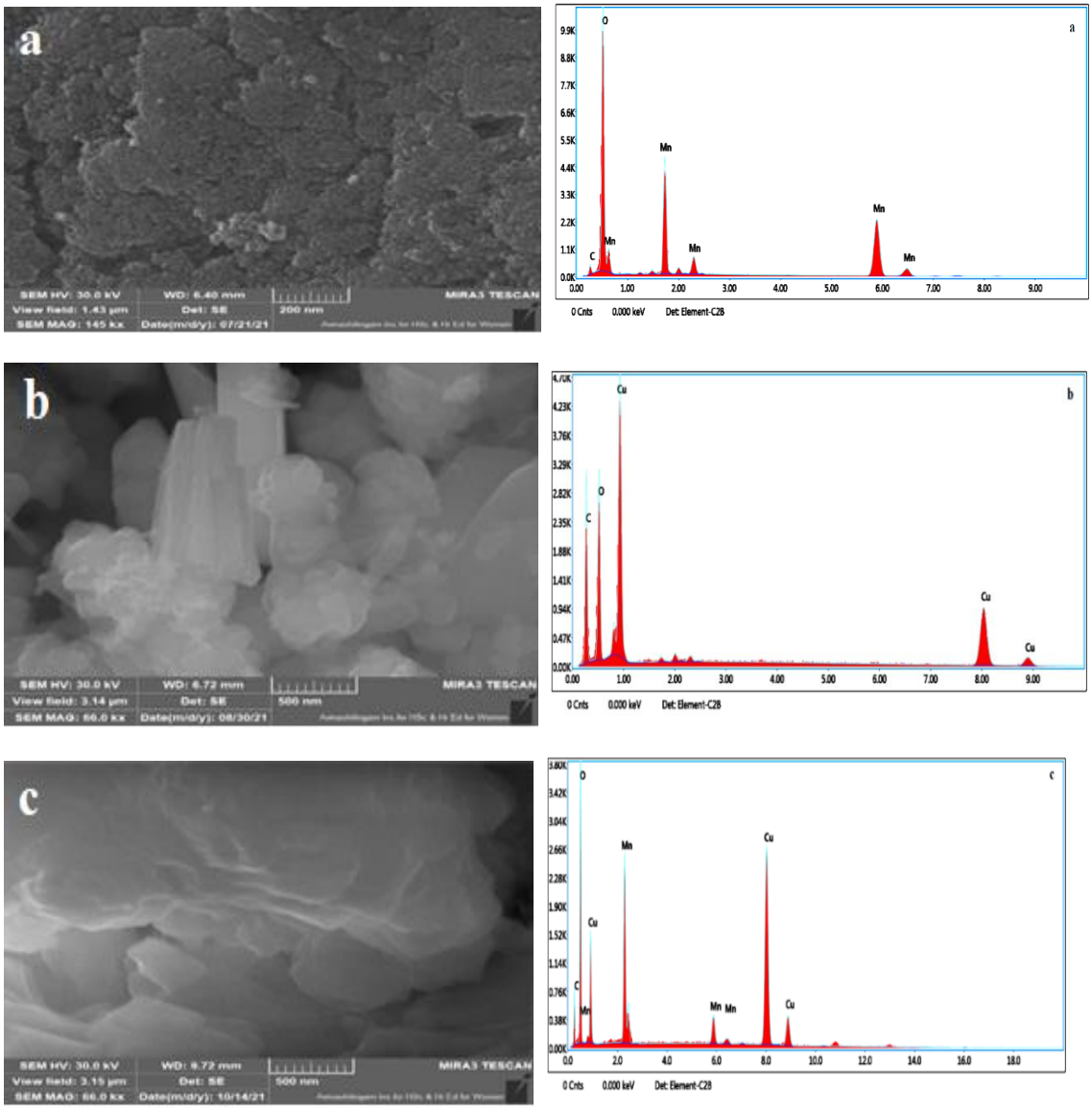

Figure 6 FE-SEM and EDX images a) Mn_2O_3, b) CuO, c) Mn-doped CuO.

Photodegradation of methylene blue (MB)

The photocatalytic activity of Mn-doped Cu oxide nanoparticles was investigated using aqueous methylene blue (MB) dye solution degradation. **Figure 7** depicts the absorption spectra of methylene blue (MB) dye as a function of wavelength (400 - 900 nm) for various time intervals using an Mn-doped Cu oxide catalyst (0, 15, 30, 45, 60, 75 and 90). Monitoring the absorption peak of methylene blue dye at 663.2 nm was used to characterize the degradation effect. The plots clearly show that the prepared Mn-doped Cu oxide nanopowders easily degrade the methylene blue dye with a slight increase in time. According to **Figure 7a**, the maximum absorption peak (at 663.2 nm) decreases with increasing irradiation time. This demonstrates that the concentration of methylene blue dye decreases in the presence of an Mn-doped Cu oxide catalyst and solar light illumination. As seen by the lower intensities of the methylene blue absorbance peak, the decreased absorption of the mixed solution was produced by the distraction of the homo and hetero-poly aromatic rings contained in the dye molecules or by the quick decomposition of methylene blue. The maximum degradation of methylene blue dye occurred in 90 min of sunlight irradiation using Mn-doped CuO catalyst at pH 7. **Figure 7b** shows the photodegradation efficiency of methylene blue at various pH levels. **Figure 7c** represents the kinetics of the MB degradation reaction in the presence of pure Mn-doped Cu oxide (prepared by synthesis). Plotting ln (C_0/C) versus t yielded a straight line. As seen in the graph, the photocatalytic methylene blue dye degradation follows first-order kinetics, as the correlation constant for the fitted line is $R^2 > 0.95$. The first-order reaction kinetics had an excellent correlation $R^2 = 0.98414$ for Mn-doped Cu oxide and the pseudo-first-order rate constants are 3.43×10^{-2} min^{-1}. The higher surface area with larger pores plays an active role in substance absorption, resulting in higher photocatalytic activity.

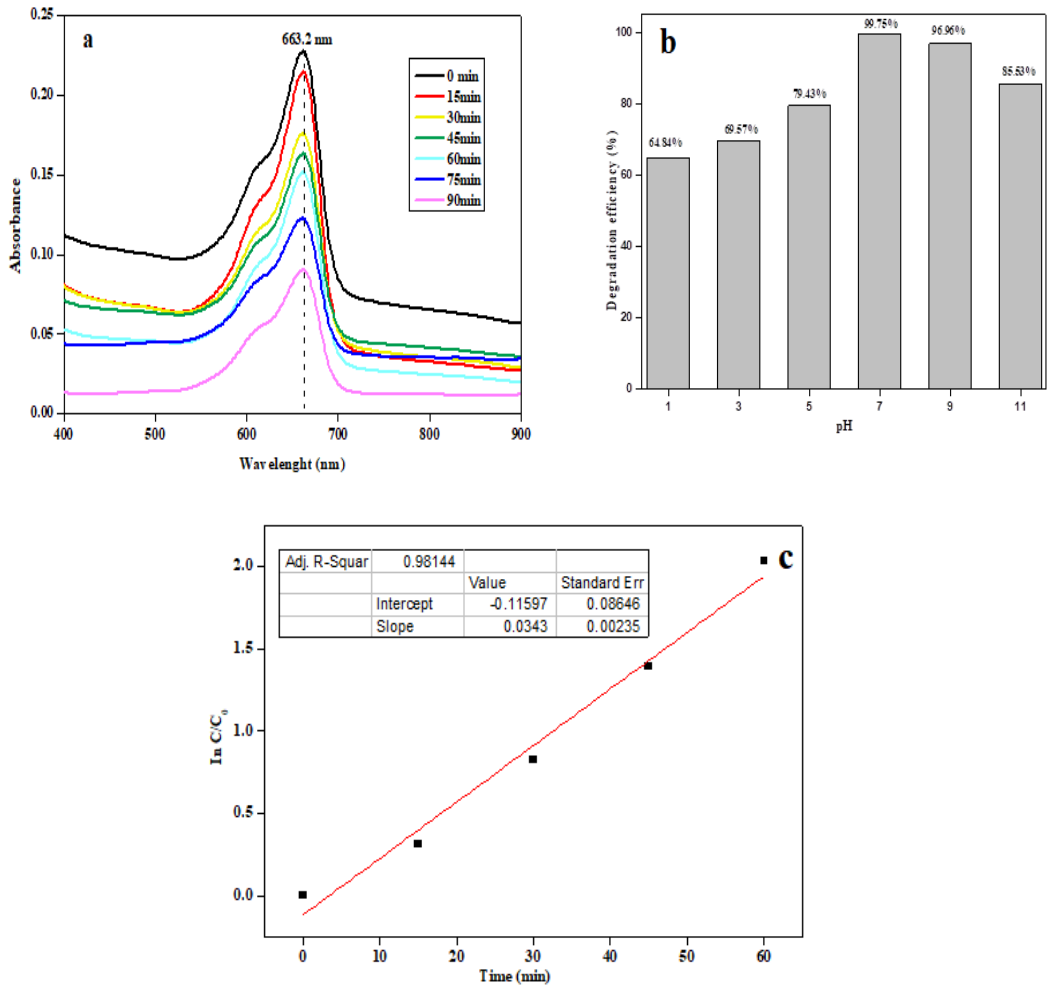

Figure 7 a) Absorbance spectra of catalyst, b) Effect of pH of dye solution, c) Pseudo-first-order rate constant (K).

Conclusions

We have successfully synthesized the Mn, Cu and Mn-doped CuO, nanoparticles by the green precipitation method, and several characterization tests confirmed the formation of nanoparticles. The XRD, UV, FTIR, FE-SEM and EDS analyses revealed that the synthesized Mn, Cu and Mn-doped Cu oxide NPs were devoid of organic substances. Other structural parameters, such as the morphology index, the number of unit cells, the x-ray density, the bulk density and so on, also show promising results. The structure and morphology of the products were investigated using FE-SEM, and EDS analysis confirmed the presence of the elements in the sample. The photocatalytic activity results show that Mn-doped CuO is better able to degrade MB due to its improved charge separation efficiency and visible light photoresponse. Interestingly, Mn-doped CuO NPs had better photocatalytic activity for the breakdown of organic dyes in wastewater.

Acknowledgement

The author is grateful to the Department of Chemistry at V.O. Chidambaram College for providing FTIR and UV. The authors are thankful to Avinashilingam University in Coimbatore for providing FESEM. The author expresses gratitude to the administration of V.O. Chidambaram College for providing the necessary supplies for this work.

References

[1] Y Liu, H Yu, Z Lv, S Zhan, J Yang, X Peng, Y Ren and X Wu. Simulated-sunlight-activated photocatalysis of Methylene Blue using cerium-doped SiO_2/TiO_2 nanostructured fibers. *J. Environ. Sci.* 2012; **24**, 1867-75.

[2] Z Aksu. Application of biosorption for the removal of organic pollutants: A review. *Process Biochem.* 2005; **40**, 997-1026.

[3] M Iqbal, A Ali, NA Nahyoon, A Majeed, R Pothu, S Phulpoto and KH Thebo. Photocatalytic degradation of organic with nanosized cadmium sulfide. *Mater. Sci. Energ. Tech.* 2019; **2**, 41-5.

[4] AF Alkaim, AM Aljeboree, NA Alrazaq, SJ Baqir, FH Hussein and AJ Lilo. Effect of pH on adsorption and photocatalytic degradation efficiency of different catalysts on removal of methyl. *Asian J. Chem.* 2014; **26**, 8445-8.

[5] M García-Mota, A Vojvodic, F Abild-Pedersen and JK Nørskov. Electronic origin of the surface reactivity of transition-metal-doped TiO_2(110). *J. Phys. Chem. C* 2013; **117**, 460-5.

[6] ME Ashebir, GM Tesfamariam, GY Nigussie and TW Gebreab. Structural, optical and photocatalytic activities of Ag-doped and Mn-doped ZnO Nanoparticles. *J. Nanomater.* 2018; **2018**, 9425938.

[7] G Viruthagiri and P Kannan. Visible light-mediated photocatalytic activity of cobalt doped Bi_2O_3 nanoparticles. *J. Mater. Res. Tech.* 2019; **8**, 127-3.

[8] X Zhang, G Zhou, H Zhang, C Wu and H Song. Characterization and activity of visible-light-driven TiO_2 photocatalysts co-doped with nitrogen and lanthanum. *Transit. Met. Chem.* 2011; **36**, 217-22.

[9] KV Kumar, K Porkodi and A Selvaganapathi. Constrain in solving Langmuir-Hinshelwood kinetic expression for the photocatalytic degradation of Auramine O aqueous solutions by ZnO catalyst. *Dyes Pigments* 2007; **75**, 246-9.

[10] AMB Leena and K Raji. Room temperature ferromagnetism in Fe doped CdS and cobalt doped CdS nano particles. *Mater. Today Proc.* 2019; **8**, 362-70.

[11] A Dhanalakshmi, B Natarajan, V Ramadas, A Palanimurugan and S Thanikaikarasan. Structural, morphological, the optical and antibacterial activity of rod-shaped zinc oxide and manganese-doped zinc oxide nanoparticles. *Pramana* 2016; **87**, 57.

[12] N Thaweesaeng, S Supankit, W Techidheera and W Pecharapa. Structure properties of As-synthesized Cu-doped ZnO nanopowder synthesized by co-precipitation method. *Energ. Procedia* 2013; **34**, 682-8.

[13] AA Barzinjy and HH Azeez. Green synthesis and characterization of zinc oxide nanoparticles using *Eucalyptus globulus* Labill. leaf extract and zinc nitrate hexahydrate salt. *SN Appl. Sci.* 2020; **2**, 991.

[14] M Sajjad, K Ali, Y Javed, A Sattar, L Akbar, A Nawaz, MZ Rashid, K Rasool and M Alzaid. Detailed analysis of structural and optical properties of spinel cobalt doped magnesium zinc ferrites under different substitutions. *J. Mater. Sci. Mater. Electron.* 2020; **31**, 21779-91.

[15] R Jacob, HG Nair and J Isac. Structural and morphological studies of nano-crystalline ceramic $BaSr_{0.9}Fe_{0.1}TiO_4$. *Int. Lett. Chem. Phys. Astron.* 2015; **41**, 100-17.

[16] Z Ullah, S Atiq and S Naseem. Indexing the diffraction patterns and investigating the crystal structure

of Pb-doped strontium ferrites. *J. Sci. Res.* 2013; **5**, 235-44.
[17] B Nath and TF Barbhuiya. Studies on the density and surface area of nanoparticles from Camellia sinensis, a natural source. *J. Chem. Pharm. Res.* 2014; **6**, 608-10.
[18] N Nagarani, P Smgcw and V Vasu. Structural and optical characterization of ZnO thin films by sol-gel method. *J. Photon. Spintron.* 2013; **2**, 19-21.
[19] SC Chopade, IG Kore, SP Patil, ND Jadhav, C Srinidhi and PA Desai. Lattice geometry controlled synthesis of Cu - Doped nickel oxide nanoparticles. *Ceram. Int.* 2018; **44**, 5621-8.
[20] GR Khan. Crystallographic, structural and compositional parameters of Cu-ZnO nanocrystallites. *Appl. Phys. A* 2020; **126**, 311.
[21] J Chauhan, R Gandhi and P Vishwavidyalaya. Synthesis and characterization of Ni and Cu Doped Zno. 2017; **1**, 26-34.
[22] SC Mali, A Dhaka, CK Githala and R Trivedi. Green synthesis of copper nanoparticles using *Celastrus paniculatus* Willd. leaf extract and their photocatalytic and antifungal properties. Biotechnol. Rep. 2020; **27**, e00518.
[23] S Sukumar, A Rudrasenan and DP Nambiar. Green-synthesized rice-shaped copper oxide nanoparticles using caesalpinia bonducella seed extract and their applications. *ACS Omega* 2020; **5**, 1040-51.
[24] X Zhang, D Zhang, X Ni and H Zheng. Optical and electrochemical properties of nanosized CuO via thermal decomposition of copper oxalate. *Solid State Electron.* 2008; **52**, 245-8.
[25] V Hoseinpour, M Souri and N Ghaemi. Green synthesis, characterisation, and photocatalytic activity of manganese dioxide nanoparticles. *Micro Nano Lett.* 2018; **13**, 1560-3.
[26] SA Khan, S Shahid, B Shahid, U Fatima and SA Abbasi. Green synthesis of MnO nanoparticles using *abutilon indicum* leaf extract for biological, photocatalytic, and adsorption activities. Biomolecules 2020; **10**, 785.
[27] SK Chandraker, M Lal, MK Ghosh, V Tiwari, TK Ghorai and R Shukla. Green synthesis of copper nanoparticles using leaf extract of *Ageratum houstonianum* Mill. and study of their photocatalytic and antibacterial activities. *Nano Express* 2020; **1**, 010033.
[28] A Jayadev and NB Krishnan. Green synthesis of copper nanoparticles and its characterization. *J. Sci. Res.* 2021; **65**, 80-4.
[29] JP Tailor, SH Chaki and MP Deshpande. Comparative study between pure and manganese doped copper sulphide (CuS) nanoparticles. *Nano Express* 2021; **2**, 010011.
[30] SK Shinde, DP Dubal, GS Ghodake, P Gomez-Romero, S Kim and VJ Fulari. Influence of Mn incorporation on the supercapacitive properties of hybrid CuO/$Cu(OH)_2$ electrodes. *RSC Adv.* 2015; **5**, 30478-84.
[31] A Suganthi, SJK Vethanathan, S Perumal, DP Koilpillai and S Karpagavalli. Optical and electrical properties of solvothermally synthesized manganese doped cuprous oxide nanoparticles. *IOSR J. Appl. Phys.* 2017; **1**, 43-8.
[32] M Souri, V Hoseinpour, A Shakeri and N Ghaemi. Optimisation of green synthesis of MnO nanoparticles via utilising/response surface methodology. *Inst. Eng. Tech.* 2018; **12**, 822-7.
[33] C Krishnaraj, BJ Ji, SL Harper and SI Yun. Plant extract-mediated biogenic synthesis of silver, manganese dioxide, silver-doped manganese dioxide nanoparticles and their antibacterial activity against food- and water-borne pathogens. *Bioproc. Biosystems Eng.* 2016; **39**, 759-72.
[34] M Kaupp, D Danovich and S Shaik. Chemistry is about energy and its changes: A critique of bond-length/bond-strength correlations. *Coord. Chem. Rev.* 2017; **344**, 355-2.
[35] RM Badger. The relation between the internuclear distances and force constants of molecules and its application to polyatomic molecules. *J. Chem. Phys.* 2004; **3**, 710.
[36] MA Farrukh, KM Butt, KK Chong and WS Chang. Photoluminescence emission behavior on the reduced bandgap of Fe doping in CeO_2-SiO_2 nanocomposite and photophysical properties. *J. Saudi Chem. Soc.* 2019; **23**, 561-75.